Quantitative assessment of preferential fatigue initiation sites in a multi-phase aluminium alloy

M. R. JOYCE[1], K. K. LEE[2], S. SYNGELLAKIS[3] and P. A. S. REED[1]

[1]Materials Research Group, School of Engineering Sciences, [2]ISIS Group, [3]Computational Engineering and Design Group, School of Engineering Sciences, University of Southampton, Highfield, Southampton, SO17 1BJ, UK

ABSTRACT   Complex multi-phase Al–Sn–Si alloys are commonly employed in the manufacture of small automotive plain bearings. The fundamental fatigue initiation behaviour of this class of alloys is currently not well understood. A range of analytical techniques were applied to investigate preferential initiation site location and to attempt to identify critical microstructural features. It was apparent from experimental studies that points of fatigue crack initiation are associated with the Si secondary phase. Using tessellation approaches and subsequently both adaptive numerical modelling and micro-scale finite element modelling allowed the identification of features affecting the probability that a given Si phase would initiate a fatigue crack.

Keywords   adaptive numerical modelling; aluminium alloys; fatigue; finite element analysis.

INTRODUCTION

Current automotive plain bearings utilize a multi-layer material system to achieve the required combination of properties to cope with the demands of modern internal combustion engines. The material system considered in this work comprises a multi-phase Al–Sn–Si lining material bonded to a steel-backing layer via a thin layer of Al foil as shown in Fig. 1a. In service, the bearing lining is loaded by pressure from the hydrodynamic oil layer, the rapidly changing nature of which leads to dynamic stress fields being evolved in the bearing.[1] Although in-service fatigue failure does not usually occur, accelerated test rigs are used to push bearings to their fatigue limits for development purposes. While these test rigs apply similar oil film loadings to service (albeit greatly increased), their design precludes the detailed surface observations required to characterize fatigue crack initiation and early growth.

The research presented in this paper focuses on the fundamental fatigue behaviour of the material system described above. Therefore, rather than considering the service loading, tests were carried out under simple and well-defined stress states. The bearing material system was available as a flat strip in the condition immediately prior

Correspondence: M. R. Joyce. E-mail: mrj1@soton.ac.uk

to the final forming operation, and standard bend bar specimens of dimensions $80 \times 20 \times 2$ mm were produced from this material. While the final forming process does introduce slight work hardening into the bearing lining, the impact on fatigue properties was found to be negligible. These samples were tested in a three-point bend with the Al alloy lining uppermost and therefore subject to maximum cyclic loading, as shown in Fig. 1b. All tests were carried out on highly polished samples using an Instron 8501 servo-hydraulic fatigue-testing machine at an R-ratio of 0.1 and at a frequency of 20 Hz. Fatigue crack monitoring was carried out using the acetate replication technique; hence reasonably short test durations were required ($<100\,000$ cycles). It was found that the loads required to reliably initiate fatigue cracks within this lifetime were such that the maximum stress level on the lining material surface was considerably above yield (an elasto-plastic FE model predicted that $\sigma_{max} = 105$ MPa, while the lining material has the properties $\sigma_{yield} = 56$ MPa and $\sigma_{UTS} = 170$ MPa). Typically, each test contained greater than 1000 fatigue crack initiation sites. However, due to the loading geometry and inter-crack shielding, many of these micro-cracks fail to propagate for any significant distance. Joyce *et al.*[2] discuss in detail the general short crack initiation and early growth behaviour observed in this material system, while this paper focuses on the application of various analytical techniques to characterize critical
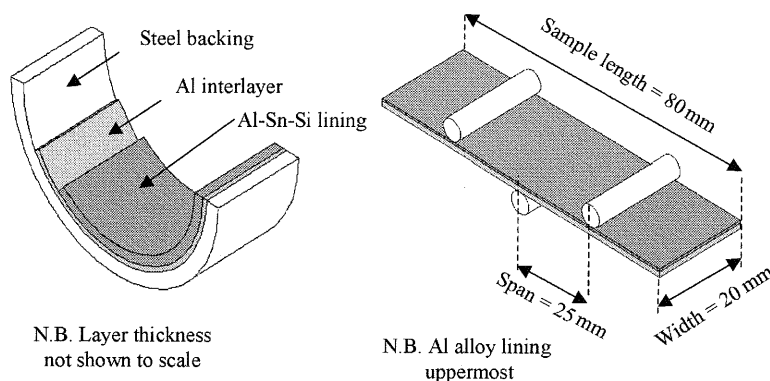
Fig. 1 (a) Schematic of shell bearing construction, (b) three point bend fatigue testing geometry.
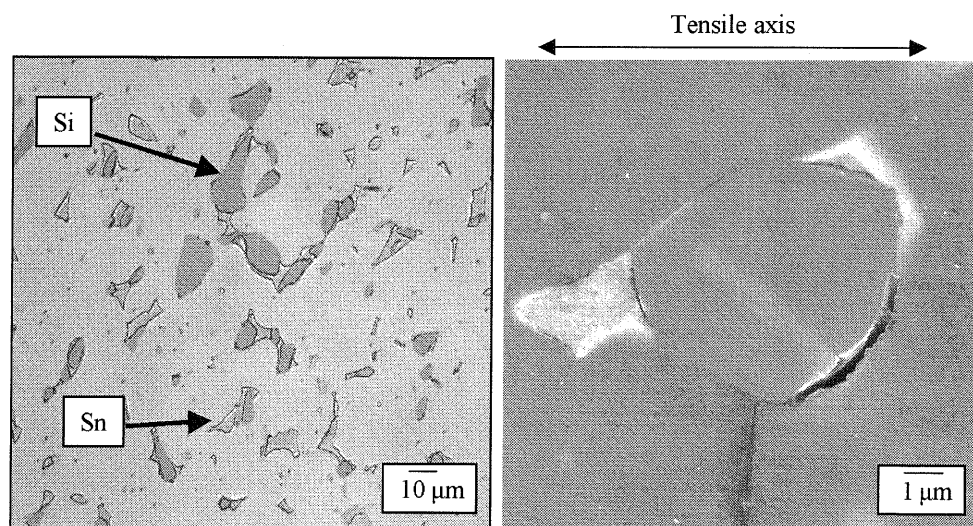

Fig. 2 (a) Optical micrograph of bearing lining microstructure, (b) FEGSEM micrograph showing typical fatigue initiation site at a debonded Si phase.

local microstructural features associated with fatigue crack initiation.

MICROSTRUCTURAL OBSERVATIONS AND ANALYTICAL METHODOLOGY

A sample section of bearing lining is shown in Fig. 2a, where it can be seen that this material is multi-phase with the Si and Sn secondary phases existing as two distinct particle distributions. It was seen that fatigue crack initiation in this material was exclusively associated with the debonding of the Si phase from the surrounding matrix as shown in Fig. 2b. This behaviour has been reported in other cast Al–Si alloys where porosity is insignificant.[3–5] Madelaine-Dupuich and Stolarz[4] saw that fatigue crack initiation was associated with the cracking or debonding of primary silicon particles. Based on their observations they postulated that large Si particles would crack, while smaller Si particles would debond. In the bearing alloy

considered here, cracking of large Si particles is unlikely as extensive rolling during the production route will have already fractured and redistributed any large brittle silicon phases present. The objective of the current work was to add to this established understanding of the role of silicon and to further consider the role of the surrounding local micro-geometry. To achieve this it is necessary to measure the microstructure in a systematic and quantitative manner. The technique applied in this case is finite body tessellation (FBT).

Tessellation approaches provide a method of statistically characterizing a multi-phase microstructure. The definition of a network of tessellated cells surrounding each particle, such that all points within a given cell are closer to the included particle than any other, has been identified by several authors[6,7] as a powerful analytical tool. The characteristics of this tessellation may be assessed as an overall distribution on a global volume or area averaged basis and the ability to quantify such parameters on a 'cell

by cell' basis allows considerable insight into nucleation type processes.

In contrast to the classical Dirichlet method, the FBT approach developed by Boselli et al.[8] is capable of generating representative tessellated structures from phase distributions containing large or elongated particles. Furthermore, because cell/particle overlaps cannot occur using the finite body approach, the cells generated by this method are far more representative of the region with which the included particles may be expected to interact. These features make the finite body approach a far more powerful tool for characterizing nucleation type events associated with individual particles.

MICROSTRUCTURAL CHARACTERIZATION

Using acetate replicas of the sample surface taken during fatigue tests, it was possible to identify areas of microstructure containing crack initiation sites. A total of 10 regions were randomly selected, each containing approximately 300 discrete Si secondary phases. Binary images including only the Si secondary phase were produced, allowing tessellated structures to be constructed using the FBT approach. The cells produced by this method were divided into three populations according to behaviour of the contained particle:

- Initiating cells—those cells containing a particle at which a fatigue crack initiated.
- Bordering cells—those cells sharing a common boundary with an initiating cell (near neighbours of initiating particles).
- Background cell—those cells neither containing nor sharing a boundary with a cell containing a fatigue crack initiation site.

Subdividing the cell population in this manner gave a total of 163 initiating, 810 bordering and 1965 background cells. The measures described below were then applied to each cell.

- Object area (OA): area of the object, i.e. Si particle.
- Object aspect ratio (OAsp): aspect ratio of the object (maximum chord length divided by maximum width perpendicular to the maximum chord length).
- Object angle (OAng): angle of the object's longest chord with respect to the tensile axis (between 0 and $\pi/2$ radians).
- Cell area (CA): area of the cell.
- Cell aspect ratio (CAsp): aspect ratio of the cell (maximum chord length divided by the maximum width perpendicular to the maximum chord length).
- Cell angle (CAng): angle of the cell's longest chord with respect to the tensile axis (between 0 and $\pi/2$ radians).
- Local area fraction (LAF): OA divided by the CA ($\times 100$).
- Number of near-neighbours (NNN): number of objects sharing a cell boundary with the object of interest.
- Nearest-neighbour distance (d_{min}): shortest interfacial distance with any of the near-neighbours.
- Mean near-neighbour distance (d_{mean}): average of interfacial distances to all of the near neighbours.
- Nearest-neighbour angle (NNAng): angle of the line joining the centroid of the object to the centroid of the nearest neighbour, measured with respect to the tensile axis (between 0 and $\pi/2$ radians).

The mean values and standard deviations of these measures are given in Table 1. First considering the OA, it was seen that mean OA (Si particle size) is considerably higher in initiating cells than bordering cells and that this in turn is higher than background cells. As shown in Fig. 3, a distinct shift in the frequency distribution was also evident. Similar observations were made for CA, where again the initiating cells were found to be generally larger than the bordering cells, and these in turn were larger than the background cells. These trends were revealed in terms of both higher mean values and as discernible shifts in the frequency distribution.

Table 1 Mean values and standard deviation for tessellation measurement on initiating, bordering and background cells

| Type	OA (μm^2)	OAsp	OAng (rad)	CA (μm^2)
Initiating	12.17 ± 11.54	1.49 ± 0.36	0.90 ± 0.41	113.65 ± 58.59
Bordering	6.22 ± 6.73	1.50 ± 0.41	0.88 ± 0.42	87.59 ± 53.45
Background	4.24 ± 5.19	1.48 ± 0.50	0.87 ± 0.4	62.46 ± 43.21
Type	CAsp	CAng (rad)	LAF	NNN
Initiating	1.48 ± 0.42	0.88 ± 0.42	10.48 ± 6.41	6.39 ± 1.38
Bordering	1.61 ± 1.22	0.79 ± 0.44	6.98 ± 5.34	6.00 ± 1.45
Background	1.70 ± 1.51	0.77 ± 0.44	6.93 ± 5.73	5.52 ± 1.42
Type	d_{mean} (μm)	d_{mean} (μm)	NNAng (rad)	
Initiating	2.61 ± 1.87	7.59 ± 2.5	0.73 ± 0.44	
Bordering	2.53 ± 1.92	7.30 ± 2.64	0.79 ± 0.46	
Background	1.94 ± 1.7	6.03 ± 2.56	0.83 ± 0.45	
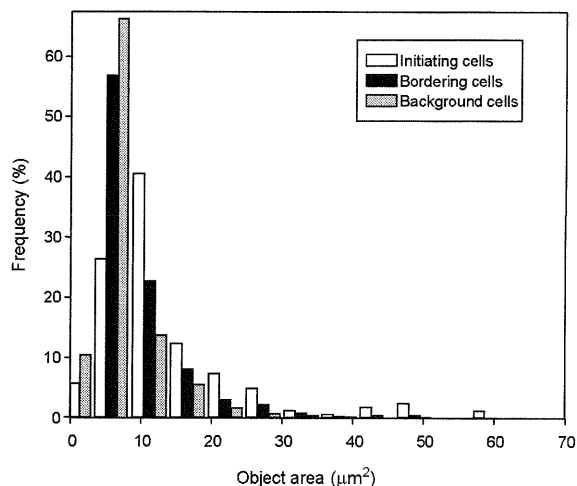
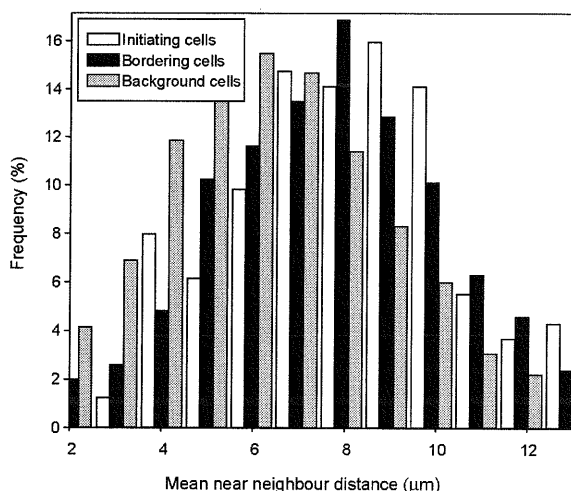**Fig. 3** Frequency distribution of object area (OA).

Fig. 4 Frequency distribution of mean near neighbour distance (d_{mean}).

The frequency distribution for d_{mean} again showed a clear shift in the distribution, as shown in Fig. 4. This indicates that Si phases associated with fatigue crack initiation are generally more remote from their immediate neighbours. In turn this may be interpreted as evidence for reduced local clustering and indicates that the nearest neighbour may exert a stronger influence over the behaviour of the central particle than in the general population. No immediately discernible differences were seen in the histograms of the angle or aspect ratio measures, other than scatter in the initiating cell distributions probably caused by the small number of initiating cells compared to the other two populations.

In summary, simple inspection of these results indicates that initiating particles tend to be larger than the back-

ground population as well as giving some indication of reduced local clustering in the initiating cell group. However, the large standard deviations associated with the mean values indicate that the groups of Si particles are not easily separable—predicting whether an individual Si particle will initiate failure from individual measurements of FBT features cannot be guaranteed.

CLASSIFICATION USING SUPANOVA

Further insight into the relationship between the assessed microstructural features and the likelihood of a given Si particle causing fatigue crack initiation may be gained from statistical classification techniques which consider combinations of FBT features. In this case a modified adaptive numerical modelling (ANM) approach, based on support vector machines (SVM), SUPANOVA[9] was applied. Unlike many classification techniques, which place an emphasis on obtaining a good classification rate (e.g. 100% successful classification of those Si phases which are associated with crack initiation), the SUPANOVA approach provides enhanced model transparency, and hence aids model interpretation (e.g. why do these phases cause initiation?). Such interpretation provides a valuable mechanistic insight, and hence allows physically based optimization of the process in question. The ability to understand the underlying model input/output relationship is often overlooked in the case of classification. The SUPANOVA technique has been extended from regression[10] to the domain of classification enabling a predictive model with a high degree of interpretability to be recovered.

As mentioned in the previous section the Si particles assessed by FBT were initially divided into three populations, namely initiating, bordering and background. However, prior inspection shows that the background and bordering populations are essentially similar and therefore may be combined. This reclassification provides two populations, one of 163 phases associated with crack initiation ('crack' class) and a background population of 2775 non-initiating phases ('non-crack' class).

Clearly the two classes are very different in size, and this represents an imbalanced dataset. It is necessary to avoid a bias operating for the more heavily represented class, and also the data imbalance itself may violate the random sampling principle assumed in ANM. One appropriate performance measure is the geometric mean (G_{mean}), which favours a balanced classification by measuring the square root of the product of the class classification rates.

SVM have gained success in recent years for many classification and regression problems.[11] The formulation embodies the principle of structural risk minimization developed by Vapnik,[12] which provides a mechanism for

Table 2 SUPANOVA terms selected (and the components thereof) and their percentage occurrence across 10 modelling runs on random partitions of training and test data

Term	Occurrence (%)	Component 1 (uv)	Component 2 (bv)	Component 3 (tv)	Initiation
1	100	CA = high			Likely
2	100	LAF = high			Likely
3	60	LAF = high	d_{mean} = high		Likely
4	80	OAng = low	CAng = low		Likely
5	80	OAng = low	NNAng = low	d_{mean} = high	Unlikely

choosing optimal model complexity for limited data and uses kernels to transform input space into high dimensional feature space. SVM produce essentially 'black box' predictive models (as do many neural networks), i.e. they can produce very accurate models, but the relationship between inputs and outputs is difficult to visualize. Transparency can be introduced by the use of the SUPANOVA framework, where an analysis of variance (ANOVA) functional decomposition of the form

$$f(x) = f_0 + \sum_{i=1}^{d} f_i(x_i) + \sum_{i=1}^{d} \sum_{j=i+1}^{d} f_{i,j}(x_i, x_j)$$

$$+ \cdots + f_{1,2,\ldots,d}(\mathbf{x}) \tag{1}$$

is used within the kernel, where $\mathbf{x} \in \mathbf{R}^d$, f_0 is the bias and the rest of the terms are univariates, bivariates, etc. In SUPANOVA, a sparse representation of these terms is then chosen to give maximum transparency without sacrificing predictive accuracy as detailed by Gunn and Brown.[9] Within the framework of SUPANOVA, the effect of imbalanced data can be handled by imposing different capacity controls for each class (C^+ and C^-), thereby effectively controlling the errors in each class. A more detailed description of the approach taken to incorporate the misclassification cost and performance criteria for imbalanced data, can be found in Lee *et al.*[13,14] This incorporates a four-stage process, i.e. (1) initial generation of an SVM model giving a good predictive performance on unseen data (good generalization) by selecting appropriate C^+ and C^- values (2) ANOVA basis selection—decomposing the complex SVM function into the full set of sub-components (3) sparse ANOVA selection—reduce the number of ANOVA terms while maintaining good generalization estimates (4) parameter selection—using the sparse model functions selected, recalculate the parameters to give good generalization.

The 11 input features (OA etc.) were normalized between 0 and 1 to avoid bias for any particular feature. After normalization, the data were partitioned into training and testing data sets. A reduced data set was considered for training, consisting of 1200 'non-crack' and 120 'crack' Si particle measurements. The rest of the data were reserved for testing the SUPANOVA models. This partitioning of

the data was repeated 10 times with random selection of the training and testing data split each time. The generalization performance of the initial SVM models was assessed, and found to be optimum with the capacity controls set to $C^+ = 10$ and $C^- = 1$, resulting in mean and variance values of $G_{mean} = 0.72$ and 0.0185, respectively, indicating consistent model predictions were being obtained from the different dataset splits.

The ANOVA expansion of the 11 tessellation features has 2048 (2^{11}) possible terms, but using the sparse representation approach adopted in SUPANOVA it was possible to reduce this to just six terms (including a bias term) without greatly compromising overall performance. The sparse model gave a successful 'crack' classification rate of 69%, a successful 'non-crack' classification rate of 71% and an overall classification performance based on mean and variance values of $G_{mean} = 0.70$ and 0.0136, respectively. The univariate (uv), bivariate (bv) and trivariate (tv) terms selected most consistently for the different data -set sampling runs are briefly summarized in Table 2.

In addition to the summary provided in Table 2, plots of the relationships found between these inputs (x-axis or x–y axes) and the likelihood of cracking (y or z-axis) are shown in Figs 5 and 6, in which a decreasing trend in the y-axis (2D) or the z-axis (3D) indicates increased probability of fatigue initiation. It can be seen in Fig. 5a that term 1 is a simple relationship between increasing CA and the increasing likelihood of the Si particle initiating a crack. Likewise term 2, shown in Fig. 5b, also shows an increasing probability of a Si particle causing fatigue initiation with increasing LAF. This may be interpreted as follows: large Si particles of high LAF are predominantly acting as fatigue initiation sites. The fact that the classifier has identified CA rather than OA explicitly, is intriguing. Due to the FBT process, the CA is directly linked to the OA (as the cell is defined as always larger than the OA). The condition that both increased CA and LAF (i.e. OA/CA) give rise to preferential crack initiation can be satisfied by considering a large OA as identifying a crack initiating particle. A large value of LAF for initiating cells may also be associated with local microstructural clustering; however, this would generally imply low values of d_{mean}, a
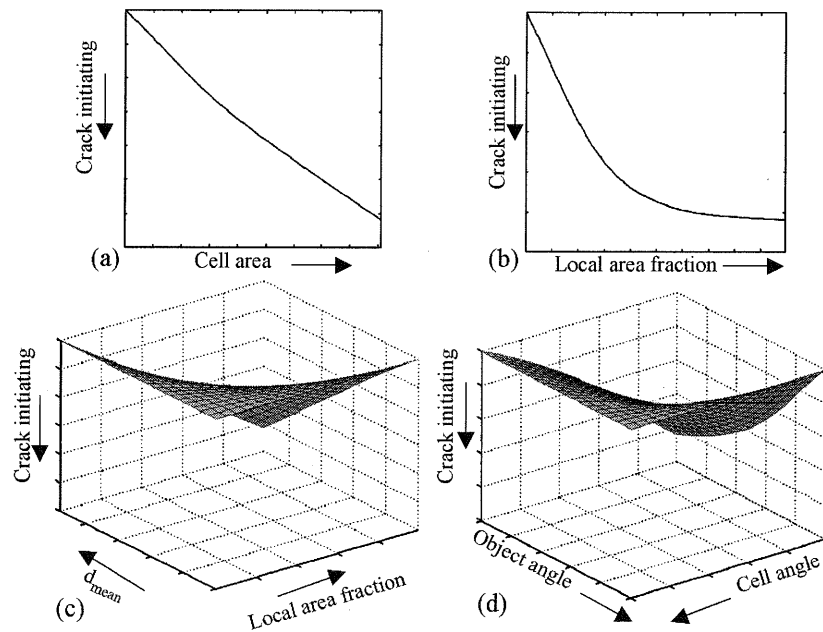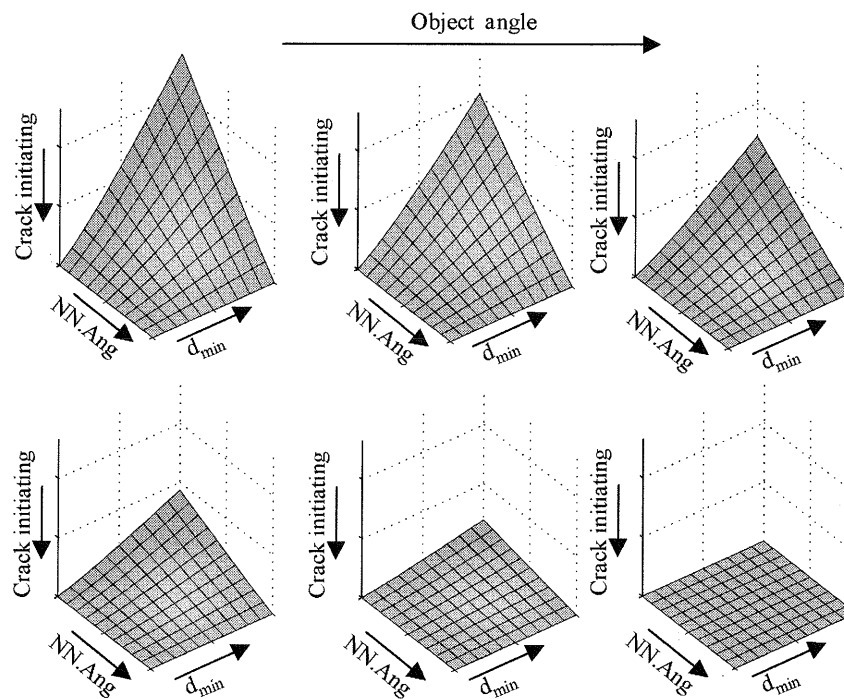
Fig. 5 ANM terms 1–4.

Fig. 6 ANM term 5.

condition contradictory to term 3, the bivariate of LAF and d_{mean} shown in Fig. 5c. There it is shown that a high d_{mean} and a high LAF are associated with Si particles causing fatigue crack initiation. A high d_{mean} may be considered to reflect a relatively unclustered local microstructure.

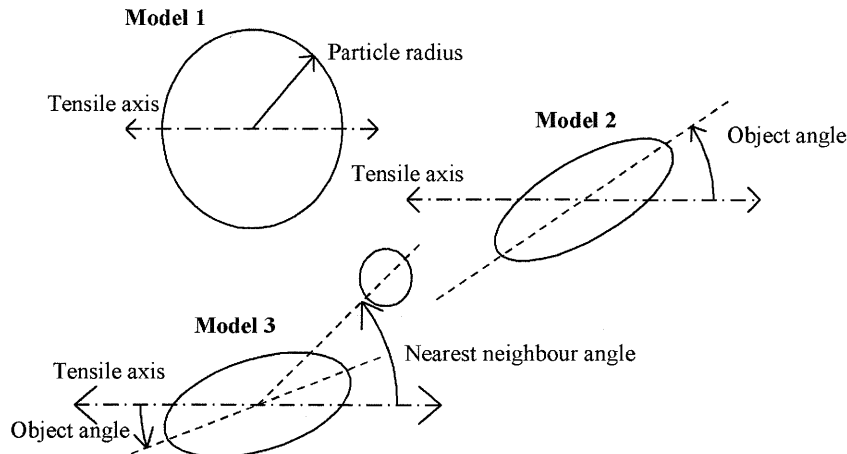The roles of the primary object and nearest neighbour orientations are addressed by term 4, the bivariate of CAng

Fig. 7 Schematics of microstructural finite element models.

and OAng (these terms may be correlated), and term 5, the trivariate of OAng, d_{min} and NNAng. The predictions of these terms, shown in Figs 5d and 6, respectively, may be interpreted as follows: fatigue initiation is likely when CAng and OAng are low (i.e. when the Si particle major axis is aligned along the tensile axis), except when d_{min} is high and NNAng is low. The selection of d_{min} and NNAng indicate that the position of the nearest neighbour may be significant in determining the behaviour of the central particle.

To summarize the interpretations from the ANM modelling, Si particles associated with fatigue crack initiation appear to be larger than average and have their major axis aligned parallel to the tensile axis. It is also indicated that fatigue cracks initiate at particles in relatively unclustered areas of local microstructure, where the position of the nearest neighbour may more strongly affect the behaviour of the central particle.

MICROSTRUCTURAL SCALE FINITE ELEMENT MODELLING

Fatigue initiation in second phase particles has been the subject of considerable research in previous years, particularly in the metal matrix composite community. During loading, complex stress fields are established around the second phase particles due to the mismatch in compliance between them and the surrounding matrix. This can cause fatigue crack initiation via particle fracture or the breakdown of the particle-matrix interface; it is this latter effect which is of more interest in the current work. Nutt and Needleman[15] first hypothesized that interfacial decohesion, and hence crack initiation occurred when the normal stress across the interface reaches a critical value. In later publications by the same authors it is assumed that cavitation would occur when the hydrostatic component of the

matrix stress state reaches a critical value.[16,17] Whitehouse and Clyne[18] experimentally observed that void nucleation sites along a particle interface correspond to points where maximum hydrostatic stress is generated, thereby adding weight to this second hypothesis. The same approach was then applied by Gall et al.[19] to investigate the initiation behaviour in Al–Si alloys.

Finite element (FE) modelling of simple particle geometries was employed to investigate any correlation between evolved matrix stress fields and the feature trends for initiation predicted by the ANM. Three models were used to characterize the effect of primary particle morphology and nearest neighbour location. These are described below and shown schematically in Fig. 7.

- Single circular particle of variable radius (effect of OA, similar to ANM term 1).
- Single elliptical particle of variable orientation with respect to the applied stress field (effect of OAng, similar to ANM term 4).
- Particle pair; central elliptical particle of variable orientation with respect to the applied stress field, a second circular particle located at variable distance and orientation (effect of d_{min}, OAng and NNAng, similar to ANM term 5)

The models were all created and solved with the ANSYS5.7 general-purpose FE code. Using a similar methodology to Dong et al.,[20] the core region in which the Si secondary phases are modelled discretely, was surrounded by a considerably larger embedding region of bulk material properties to provide appropriate constraint. It was assumed that due to its high yield stress the Si would remain elastic throughout the analysis, hence this phase was assigned the following properties:[21] $E = 400$ GPa, $v = 0.17$. While the Sn phase was not modelled discretely, because it does not appear to contribute directly to the

fatigue initiation process, its presence was accounted for in the multi-linear hardening curves for the Al–Sn–Si embedding region and the Al–Sn intra-core matrix shown in Fig. 8. These curves were produced experimentally from monotonic tensile tests, and therefore cyclic material response is not considered in this analysis. Isotropic material response was assumed, while a degree of local anisotropy will undoubtedly occur, it can be reasonably ignored, because only stress trends rather than explicit values were recovered. Monotonic loading was applied via a uniform nodal displacement, simulating an arbitrary total strain of 0.2%, which is similar to the strain levels applied during the fatigue tests.
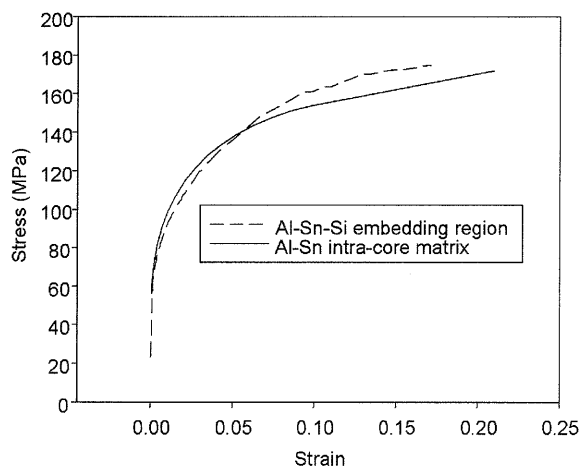

Fig. 8 Isotropic hardening curves for Al–Sn–Si and Al–Sn matrix.

Effect of particle size

Due to the symmetry of the variable particle size model, it was possible to model only a quarter of the total structure. The resultant model is shown in Fig. 9a, the radius of the central Si particle was varied from 0.5 to 4 μm, while the size of the core regions remained fixed throughout the analysis. The model was meshed using 6480 8-noded quadrilateral elements formulated for plane stress (free surface). As shown in Fig. 9b, the mesh was refined such that 160 elements were defined along the length of the Si-matrix interface (the absolute size of these elements varied from 0.005 to 0.04 μm depending on the Si particle radius). The maximum hydrostatic and principal stresses in the intra-core matrix were evaluated at each increment of particle radius. It was found that the maximum hydrostatic stress was always evolved at the same point (at the particle interface, parallel to the tensile axis), whereas the point of maximum first principal stress moved relative to the tensile axis from 33° at low particle size to 38° at the highest particle radius. This effect is due to a combination of the plastic flow at the particle interface and the changing volume fraction due to the non-infinite matrix. Figure 10 shows the variation in maximum hydrostatic stress, the first principal stress evolved at the point of maximum hydrostatic stress and the maximum first principal stress. While there is indeed some variation in the maximum hydrostatic stress, it does not show a clear trend and is likely to be influenced by the same factors causing the shift in maximum first principal stress position. In common with the results of Gall *et al.*,[19] the increase in hydrostatic stress with particle size appears negligible
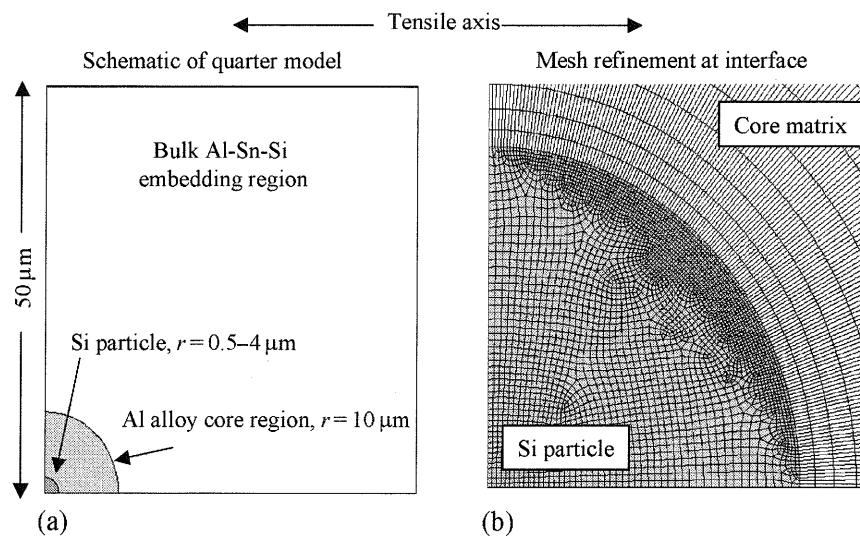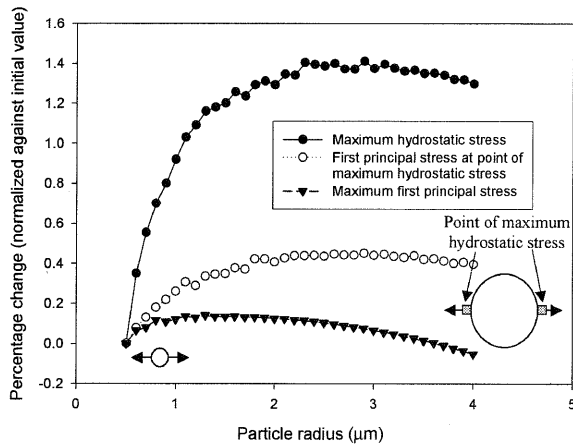

Fig. 9 Particle size model geometry.

Fig. 10 Effect of particle size on intra-core hydrostatic and first principal stresses.

Fig. 12 Effect of particle orientation on intra-core hydrostatic and first principal stresses.
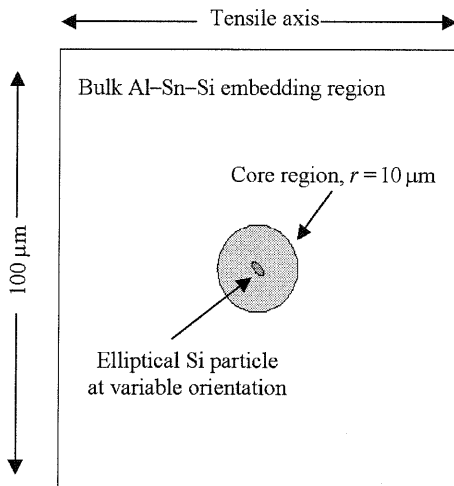

Fig. 11 Schematic of elliptical particle geometry.

and therefore appears unlikely to effect the likelihood of fatigue initiation at a given particle.

Effect of particle orientation

Unlike the previous case the geometry chosen to model the effect of particle orientation is not symmetric, hence a full rather than quarter model was required. The model shown in Fig. 11 comprises a single elliptical inclusion of fixed size representative of the upper end of the measured OAsp band (OAsp = 2), the long and short axis lengths being 4 and 2 μm, respectively. As previously the mesh is refined along the particle interface, although the particle size (and hence volume fraction) is fixed, the element length remains at 0.0125 μm in all cases. The model was meshed with 8650 8-node quadrilateral elements formu-
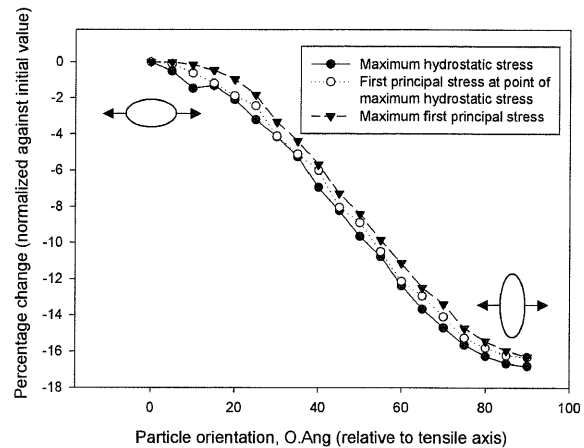
lated for the plane-stress state. The particle orientation relative to the tensile axis was varied from 0° to 90° in 5° increments; as previously, loading was applied via direct nodal displacement to simulate a 0.2% strain, while the hydrostatic and first principal stresses evolved in the intra-core matrix were recorded at each increment.

Figure 12 shows the variation in maximum hydrostatic stress, the first principal stress evolved at the point of maximum hydrostatic stress and the maximum first principal stress. In contrast to the particle size case, a strong trend is evident, clearly the hydrostatic stress is maximized when the particle is aligned such that its major axis is parallel to the applied tensile stress. This result correlates well with the ANM predictions (term 4).

Effect of near neighbour distance and orientation

To investigate the role of the near neighbour, a second particle of radius 1 μm was added to the previous model. The model was formulated such that d_{min} and NNAng in addition to OAng, were variable. Other than the addition of the second particle the model was left unchanged. The particle pair model is more complex because it contains three variables rather than one. Figure 13 shows the variation in maximum intra-core matrix hydrostatic stress from a series of solutions where OAng was fixed parallel to the tensile axis (condition most unlikely to cause initiation according to term 5) and d_{min} and NNAng varied. It appears that when NNAng is high, d_{min} has little effect on the hydrostatic stress. Similarly when d_{min} is high, NNAng has little effect. A further series of hydrostatic stress solutions, shown in Fig. 14, were obtained in which NNAng was fixed parallel to the tensile axis (condition most unlikely to cause initiation according to ANM term 5) and d_{min} and OAng varied. It can be seen that the interface
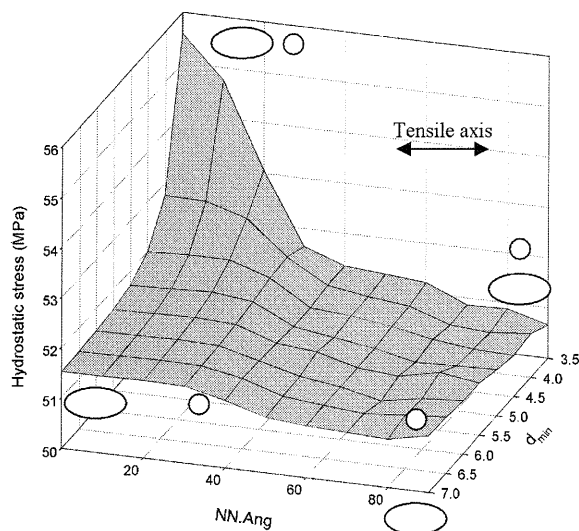
Fig. 13 Effect of nearest neighbour distance and orientation, given object angle = 0 on maximum intra-core hydrostatic stress.
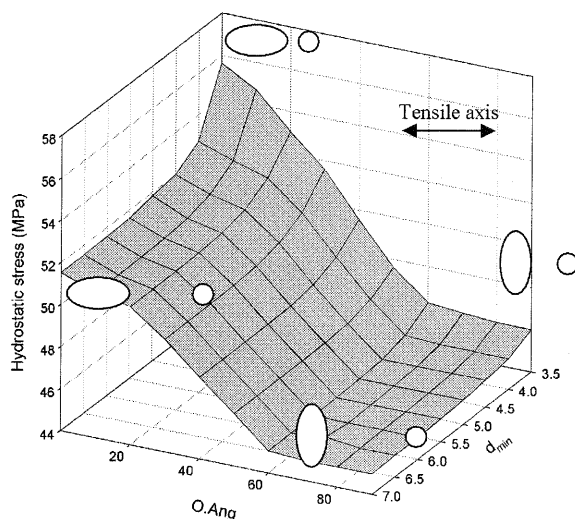

Fig. 14 Effect of nearest neighbour distance and object angle, given nearest neighbour angle = 0 on maximum intra-core hydrostatic stress.

hydrostatic stress is apparently unaffected by d_{min} when OAng is high. Furthermore when OAng is low (condition most unlikely to cause initiation according to ANM term 5), hydrostatic stress is predicted to decrease with increasing d_{min}.

Referring to Figs 6, 13 and 14, some degree of correlation is seen between the particle pair model and the ANM term 5. The FE analysis shows that a high value of d_{min} in combination with low OAng and NNAng greatly reduces the hydrostatic stress at the interface around the particle.

It is however intriguing that ANM term 5 should select OAng low to be associated with a greater probability of non-initiation, because this trend is contradictory to both ANM term 4 and the associated FE. It should be remembered that the SUPANOVA terms are additive (although not directly so), and hence this may be explained by hypothesizing that given a high d_{min} initiation is so unlikely that the roles of both OAng and NNAng become negligible, thus counterbalancing the expected effect of OAng. It is both clear from Fig. 13 that in terms of hydrostatic stress NNAng is insignificant and from Fig. 14 that the role of OAng is less pronounced, when d_{min} is large. It is possible that the trends identified in these components by the ANM may not be physically significant when applied to simple particle pairs, but represent more complex inter-relationships for particle distributions. Alternatively, these anomalous trends may be merely statistical artefacts picked out from these sets of training data.

DISCUSSION

Both simple inspection and ANM term 1 showed that larger Si particles are more likely to be associated with crack initiation. Researchers considering Al–SiC metal-matrix composites have reported similar findings.[22–24] The SiC particles in these studies were generally larger than the Si secondary phases considered here and crack initiation was associated with particle cracking rather than decohesion. However, larger particles were clearly shown to be more deleterious. Kumai *et al.*[23] report that in the absence of large cracked SiC, crack initiation is likely to occur by debonding from smaller particles in a similar manner to that observed by Madelaine-Dupuich and Stolarz.[4] It seems reasonable to assume that a similar size dependency will exist for crack initiation via debonding. In common with the work of Gall *et al.*,[19] the FE model of matrix-hydrostatic stress considered in this work shows no dependency on particle size. However, Fan *et al.*[25] performed a FE study to assess the accumulation of plasticity at inclusions in Al–Si alloys. Employing a Coffin-Manson law to correlate cyclic plastic shear strain with crack nucleation life, they showed that the number of cycles required for crack initiation was reduced as the particle size was increased.

An alternative explanation is that large particles formed during solidification and not broken up during the forming process are not well rounded and hence more prone to suffer local stress concentrations. However, the severity of cold rolling during the manufacture of the bearing lining would be expected to break up large irregular Si phases, and indeed the Si population was observed to be well rounded. A more probable explanation is that the probability of a given particle interface containing a flaw increases in proportion to its length and hence to the

particle size. Such arguments have been proposed during 'weakest link' type models. Wallin et al.[26] found that the fracture of copper oxide particle in a copper matrix under monotonic tensile loading could be adequately predicted by assuming that particle fracture is stress controlled and that particle fracture strength is inversely proportional to particle size.

In contrast to the results for particle size effects, excellent correlation was seen between the ANM term 3 and the FE approaches for the single particle orientation case. The magnitude of the hydrostatic stress evolved at the particle interface depends strongly upon its orientation with respect to the applied stress field. This effect is unlikely to be of great importance in the alloy studied because generally the Si secondary phases are well rounded and randomly aligned. However, it indicates that crack-nucleation life may be significantly shortened in microstructures containing elongated particles, particularly if due to processing or other factors many of these particles are aligned with the applied stress field.

The particle pair model confirmed that the position of the nearest neighbour strongly affects the interfacial hydrostatic stress of the central particle. It was shown that particle interaction and consequent amplification of the central particle interfacial hydrostatic stress was minimized when d_{min} was large; a condition under which it was also found that NNAng was insignificant and the effect of OAng greatly reduced. Broadly these trends correlate with ANM term 5. However, the FE results apparently show that d_{min} is far more significant than NNAng and OAng in determining non-initiation for a simple particle pair situation. Therefore, particle pairs exhibiting low d_{min} are associated with high levels of matrix hydrostatic stress and are potentially more likely to be associated with fatigue crack initiation. This implies that microstructures comprising paired or clustered secondary-phase distributions may be inherently less fatigue resistant than well-distributed arrangements.

CONCLUSIONS

The effect of local micro-geometry on preferential fatigue initiation sites in a multi-phase-bearing alloy was investigated using three numerical techniques. FBT and subsequent adaptive numerical classification were employed to recover statistical trends identifying initiating and non-initiating features. Microstructural FE modelling was then employed to investigate any correlation between predicted initiation probability and the magnitude of the local stress field. However, the combination of experimental observations, ANM and FE modelling has provided a useful insight into the morphology of microstructural features potentially deleterious to fatigue initiation. In the alloy studied, these features include the following:

- Large particles.
- Particles whose long axis was aligned with the tensile axis.
- Closely paired or clustered particles, particularly if aligned along the tensile axis.

These predictions provide a valuable insight to the identification of microstructural features apparently critical for fatigue initiation in this class of alloy, indicating that a microstructure comprising small, rounded and well-distributed secondary phases may offer potentially enhanced fatigue resistance. However, some caution must be exercised when interpreting these analyses, because they are restricted to two-dimensional sections and in the FE models to highly idealized secondary phase distributions.

Acknowledgements

REFERENCES

1 Gyde, N. (1969) Fatigue fracture in babbit lined journal bearings. *PhD Thesis*, Technical University of Denmark, Copanhagen, Denmark.

2 Joyce, M. R., Syngellakis, S. and Reed, P. A. S. (2004) Fatigue crack initiation and early growth in a multi-phase Al alloy included in a multi-layer material system. *Mater. Sci. Technol.* **20**, 47–56.

3 Hoskin, G. A., Provan, J. W. and Gruzleski, J. E. (1988) The *in-situ* fatigue testing of a cast aluminium–silicon alloy. *Theor. Appl. Fract. Mech.* **10**, 27–41.

4 Madelaine-Dupuich, O. and Stolarz, J. (1996) Fatigue of eutectic Al–Si alloys. *Mater. Sci. Forum* **217–222**, 1343–48.

5 Inguanti, P. C. (1985) Cast aluminium fatigue property/microstructure relationships. *Proceedings of the 17th National SAMPE Technical Conference*, SAMPE, Covina, CA, USA, pp. 61–72.

6 Wray, P. J., Richmond, O. and Morrison, H. L. (1983) Use of the Dirichlet tessellation for characterising and modelling non-regular dispersions of second phase particles. *Metallography* **16**, 39–58.

7 Shehata, M. T. and Boyd, J. D. (1988) Measurement of spatial distribution of inclusions. In: *Inclusions and Their Influence on Material Behaviour* (Edited by Rungla, R.). ASM International, pp. 121–31.

8 Boselli, J., Pitcher, P. D., Gregson, P. J. and Sinclair, I. (1999) Secondary phase distribution analysis via finite body tessellation. *J. Microsc.* **195**, 104–12.

9 Gunn, S. and Brown, M. (1999) SUPANOVA: A sparse, transparent modelling approach. In: *Proceedings of the IEEE International Workshop on Neural Networks for Signal Processing* (Edited by Hu, Y.-H., Larsen, J., Wilson, E. and Douglas, S.). IEEE, Piscataway, NJ, USA, PP. 21–30.

10 Femminella, O. P., Starink, M. J., Gunn, S. R., Harris, C. J. and Reed, P. A. S. (2000) Neurofuzzy and SUPANOVA modelling of structure-property relationships in Al–Zn–Mg–Cu alloys. *Mater. Sci. Forum* **331**, 1255–60.

11 Burges, C. (1998) A tutorial on support vector machines. *Data Mining and Knowledge Discovery* **2**, 121–67.

12 Vapnik, V. (1995) *The Nature of Statistical Learning Theory.* Springer-Verlag, Berlin.

13 Lee, K. K., Harris, C. J., Gunn, S. R. and Reed, P. A. S. (2001) Regression models for classification to enhance interpretability. In: *Proceedings of the 3rd International Conference on Intelligent Processing and Manufacturing of Materials, IPMM'01: Richmond, BC, CD ROM* (Edited by Meech, J. A., Veiga, M. M., Veiga, S., Maguire, J. and LeClair, S. R.), CRC Press, Boca Raton, FL, USA.

14 Lee, K. K., Harris, C. J., Gunn, S. R. and Reed, P. A. S. (2001) Classification of imbalanced data with transparent kernels. In: *Proceedings of the International Joint Conference on Neural Networks IJCNN'01* (Edited by Marko, K. and Webos, P.), IEEE, Piscataway, NJ, USA, pp. 2410–15.

15 Nutt, S. R. and Needleman, A. (1987) Void nucleation at fiber ends in Al–SiC composites. *Scr. Metall.* **27**, 705–10.

16 Llorca, J., Needleman, A. and Suresh, S. (1991) An analysis of the effects of matrix void growth on deformation and ductility in metal-ceramic composites. *Acta Metall. Mater.* **39**, 2317–35.

17 Christman, T., Needleman, A. and Suresh, S. (1991) An experimental and numerical study of deformation in metal-ceramic composites. *Acta Metall. Mater.* **37**, 3029–50.

18 Whitehouse, A. F. and Clyne, T. W. (1995) Critical stress criteria for interfacial caviation in MMCs. *Acta Metall. Mater.* **43**, 2107–14.

19 Gall, K., Horstmeyer, M., Mcdowell, D. L. and Fan, J. (2000) Finite element analysis of the stress distributions near damaged Si particle clusters in cast Al–Si alloys. *Mech. Mater.* **32**, 277–301.

20 Dong, M. and Schmauder, S. (1996) Modelling of metal matrix composites by a self consistent embedded cell model. *Acta Mater.* **44**, 2465–78.

21 Ross, R. B. (1992) *Metallic materials Specification Handbook*, 4th edn. Chapman and Hall, London.

22 Hall, J. N., Jones, J. W. and Sachdev, A. K. (1994) Particle size, volume and matrix strength effects on fatigue behaviour are particle fracture in 2124 aluminium–SiC$_p$ composites. *Mater. Sci. Engng.* **A183**, 69–80.

23 Kumai, S., King, J. E. and Knott, J. F. (1990) Short and long fatigue crack growth in a SiC reinforced aluminium alloy. *Fatigue. Fract. Engng. Mater. Struct.* **13**, 511–24.

24 Tokaji, K., Shiota, H. and Kobayashi, K. (1999) Effect of particle size on fatigue behaviour in SiC particulate-reinforced composites. *Fatigue. Fract. Engng Mater. Struct.* **22**, 281–8.

25 Fan, J., McDowell, D. L., Horstemeyer, M. F. and Gall, K. (2003) Cyclic plasticity at pores and inclusions in cast Al–Si alloys. *Engng Fract. Mech.* **70**, 1281–1302.

26 Wallin, K., Saario, T. and Torronen, K. (1987) Fracture of brittle particles in a ductile matrix. *Int. J. Fract.* **32**, 201–09.